Recirculation zones induce non-Fickian transport in three-dimensional periodic porous media

Recirculation zones induce non-Fickian transport in three-dimensional periodic porous media

Eleonora Crevacore, Tiziana Tosco, and Rajandrea Sethi*
Department of Environment, Land and Infrastructures, Politecnico di Torino, 10129 Torino, Italy

Gianluca Boccardo† and Daniele L. Marchisio
Department of Applied Science and Technology, Politecnico di Torino, 10129 Torino, Italy
(Received 23 June 2016; revised manuscript received 16 September 2016; published 23 November 2016)

In this work, the influence of pore space geometry on solute transport in porous media is investigated performing computational fluid dynamics pore-scale simulations of fluid flow and solute transport. The three-dimensional periodic domains are obtained from three different pore structure configurations, namely, face-centered-cubic (fcc), body-centered-cubic (bcc), and sphere-in-cube (sic) arrangements of spherical grains. Although transport simulations are performed with media having the same grain size and the same porosity (in fcc and bcc configurations), the resulting breakthrough curves present noteworthy differences, such as enhanced tailing. The cause of such differences is ascribed to the presence of recirculation zones, even at low Reynolds numbers. Various methods to readily identify recirculation zones and quantify their magnitude using pore-scale data are proposed. The information gained from this analysis is then used to define macroscale models able to provide an appropriate description of the observed anomalous transport. A mass transfer model is applied to estimate relevant macroscale parameters (hydrodynamic dispersion above all) and their spatial variation in the medium; a functional relation describing the spatial variation of such macroscale parameters is then proposed.

DOI: 10.1103/PhysRevE.94.053118

I. INTRODUCTION

The study of fluid flow and transport in porous media is of pivotal importance, as it finds application in a variety of fields, notably the investigation of remediation techniques for contaminated aquifers [1–6], the design of packed bed reactors and filters [7–12], enhanced oil recovery [13], and thermoradiotherapy [14,15]. Pore-scale numerical simulations can effectively be used to quantitatively assess the key processes controlling flow and transport phenomena [16–19]. A variety of upscaling techniques are available to extrapolate macroscale data from simulations and compare them with observations from laboratory and field experiments. The purpose of this work is to explore the influence of pore geometry and flow configuration on the transport of dissolved species in porous media. To complete the analysis, the evaluation of macroscale parameters is presented.

The dispersion coefficient is a key macroscale parameter expressing the dependency of transport on pore-scale features [20,21] and as such its *a priori* evaluation has been the subject of many investigations. The problem of quantifying dispersion in porous media is often studied within the same theoretical framework both for molecular solutes and solid particles: therefore, in this article we will refer to both scenarios.

A common way to model the macroscale dispersion flux is that of describing it as Fickian, following the Taylor-Aris model [22,23]. Under this assumption, transport is defined by the advection-diffusion equation (ADE). Nonetheless, data demonstrate that this assumption is not suitable to describe systems subject to tailing effects, nor systems for which the time scales of interest are much shorter than the characteristic diffusive time (i.e., preasymptotic effects have to be considered). Hereafter, when the Fickian assumption fails to describe transport phenomena, the terms non-Fickian or anomalous transport will be used.

As summarized by Perkins, Carrera, and Delgado [24–26], several studies have been devoted to the analysis of dispersion in porous media and to the formulation of appropriate macroscale models able to describe non-Fickian transport. The family of mass transfer models (MTs) has enjoyed particular success. By adopting a first-order mass transfer model, the medium is partitioned into a mobile region, where transport takes place both by advection and diffusion, and an immobile or stagnant zone, in which diffusion is the only transport mechanism [27–29]. In recent years, the continuous time random walk method (CTRW) [30–33] has been proven to be particularly effective in tackling the problem of non-Fickian transport. The solute is described as a finite number of particles, whose movements are described as random walks [34]. CTRW has been extensively adopted to investigate non-Fickian transport within both realistic [35,36] and simplified two-dimensional (2D) periodic media [37,38], as it is possible to derive reliable macroscopic transport equations. Especially in the case of 2D geometries, researchers' attention focused on flow field characteristics and the presence of recirculation zones was identified as a possible source of anomalous transport.

The phenomenon of recirculation itself was described in few studies: Davis *et al.* [39] evinced that when two spheres are aligned in the main flow direction, the distance between them is one of the main features influencing the recirculation topology. Experimental visualization of this phenomenon was provided by Taneda [40]. Dealing with three-dimensional (3D) packings, these results cannot be applied in a straightforward manner. Thus, the formation of recirculation zones in 3D periodic media at moderate and high Reynolds numbers was numerically investigated by several authors [41–44].

In this work, the formation of recirculation zones and their impact on solute transport is studied under creeping flow

*rajandrea.sethi@polito.it
†Present affiliation: School of Mechanical Engineering, Tel Aviv University, Tel Aviv, 69978, Israel.

conditions (i.e., laminar flow with negligible inertial forces), with flow velocities compatible with environmental applications. At the pore scale, the problem is investigated in 3D periodic media constituted by grains of equal size and shape placed along spatially periodic arrangements. Periodic structures were chosen since they represent an appropriate tradeoff between limited computational costs and a satisfactory representation of realistic systems [45]. Most of the configurations investigated in the literature are cubic arrangements inspired by crystal structures: in this work the face-centered-cubic (fcc), body-centered-cubic (bcc), and the sphere-in-cube (sic) structures are employed.

The first part of the study is focused on the complete characterization of 3D recirculation zones and on how this phenomenon unexpectedly arises even at very low Reynolds numbers. The second part aims to quantitatively assess how pore-scale structure and flow field configuration impacts on the anomalous transport observed at the macroscale. The results of the pore-scale simulations are interpreted in terms of breakthrough curves and analyzed to derive relevant macroscale parameters. The macroscale model adopted to interpret the data is based on the dual-porosity model (DP), with nonconstant parameters in order to heuristically capture the spatial variation of the transport phenomena at the time scales preceding the asymptotic conditions. In particular, the macroscale parameters are described as functions of the space variable: the novel type of functional dependence proposed in this work proves to be appropriate under all the operating conditions and for all the geometrical configurations investigated.

II. GOVERNING EQUATIONS

The flow field within the porous medium can be determined by solving the well-known Navier-Stokes and continuity equations at the pore scale which, under steady-state conditions, read as follows:

$$\rho\,\mathbf{u}\cdot\nabla\mathbf{u} = -\nabla p + \mu\Delta\mathbf{u}, \tag{1}$$

$$\nabla\cdot\mathbf{u} = 0, \tag{2}$$

where ρ is the density of the fluid (water in this study) ($\mathrm{kg\,m^{-3}}$), $\mathbf{u}$ is the effective velocity ($\mathrm{m\ s^{-1}}$), p is the pressure ($\mathrm{kg\,m^{-1}\,s^{-2}}$), and μ is the fluid dynamic viscosity ($\mathrm{kg\,m^{-1}\,s^{-1}}$). The Reynolds number associated to the problem is $\mathrm{Re} = d_g u\rho/\mu$, where the characteristic length d_g is the grain diameter (m) and u is the characteristic velocity ($\mathrm{m\,s^{-1}}$), as defined in the Appendix.

In the sections that follow, the angle θ between velocity $\mathbf{u}$ and vorticity $\boldsymbol{\omega} = \nabla\times\mathbf{u}$ will be of particular interest. Since in 3D flow $\mathbf{u}$ and $\boldsymbol{\omega}$ are not perpendicular (whereas they are in a 2D configuration), the angle θ formed by these two vectors is a good indicator of the tendency of fluid streaklines to present helical trajectories [41]; for this reason in the case of inviscid fluids, the quantity $\int_V \mathbf{u}\cdot\boldsymbol{\omega}\,dV$ is known as helicity [46]. θ is given by

$$\theta = \arccos\left(\frac{\boldsymbol{\omega}\cdot\mathbf{u}}{|\boldsymbol{\omega}||\mathbf{u}|}\right), \tag{3}$$

and when it is close to 0° or 180° the fluid flow tends to bend and present helical trajectories.

In numerous applications, the transported species are molecular solutes or very fine colloidal particles, that exhibit negligible inertial effects and undergo Brownian motion. Under these conditions, both molecular solutes and colloidal particles can be described by solving, at the pore scale, the classical advection-diffusion equation:

$$\frac{\partial c}{\partial t} + \mathbf{u}\cdot\nabla c = D_0\nabla^2 c, \tag{4}$$

where c is the solution concentration in the liquid phase ($\mathrm{mol\,m^{-3}}$), $\mathbf{u}$ is the velocity field obtained solving Eqs. (1) and (2), and D_0 ($\mathrm{m^2\,s^{-1}}$) is the diffusion coefficient. In the case of a diluted suspension of colloidal particles, D_0 is obtained with the well-known Stokes-Einstein equation [47] $D_0 = \kappa T/(3\pi\mu d_p)$, where κ is the Boltzmann constant ($\mathrm{m^2\ kg\,s^{-2}\,K^{-1}}$), T is the temperature (K), and d_p is the colloidal particle diameter (m). In this case, the Péclet number $\mathrm{Pe}_0 = d_g u/D_0$ is the relevant dimensionless number.

Aside from studying transport at the pore scale, it is also necessary to develop a framework for its investigation at the macroscale. In this context, several models are available, such as the aforementioned first-order mass transfer models (MTs); hereafter, adopting the mobile-immobile model, we will refer to it as dual-porosity model (DP). The upscaling procedure to move from the pore scale to the macroscale often involves a dimensionality reduction from three to one dimension, where only the main flow direction x is considered. The one-dimensional (1D) DP equations read as follows:

$$\varepsilon_m\frac{\partial C_m}{\partial t} + q\frac{\partial C_m}{\partial x} = \frac{\partial}{\partial x}\left(\varepsilon_m D_H\frac{\partial C_m}{\partial x}\right) - \chi(C_m - C_{im}),$$
$$\varepsilon_{im}\frac{\partial C_{im}}{\partial t} = \chi(C_m - C_{im}), \tag{5}$$

where the subscript m refers to the mobile liquid phase, while im refers to the immobile (i.e., stagnant) liquid region; ε_m, ε_{im} are the porosity values (i.e., volume of the fluid phase considered over total volume of the porous medium) and they sum up to the total (geometrical) porosity $\varepsilon = \varepsilon_m + \varepsilon_{im}$, q is the Darcyan velocity ($\mathrm{m\,s^{-1}}$), C is the macroscale fluid concentration per total liquid volume ($\mathrm{mol\,m^{-3}}$), D_H is the macroscale dispersion coefficient ($\mathrm{m^2\,s^{-1}}$), and χ is the exchange coefficient ($\mathrm{s^{-1}}$) between mobile and immobile regions. These equations follow the DP model base assumption that advection and dispersion take place together only in the mobile region, while diffusion is the only active mechanism in the immobile phase. The dimensionless parameters characterizing the DP model are $\beta = \varepsilon_m/\varepsilon$, $\phi = \chi d_g/q$, and the macroscale Péclet number $\mathrm{Pe}_H = q d_g/(\varepsilon_m D_H)$, as evident from the dimensionless form of Eq. (5) reported in the Appendix. When the volume of the immobile region is negligible, and the dispersive transport is Fickian, Eq. (5) reduces to the advection-dispersion model (ADE)

$$\varepsilon\frac{\partial C}{\partial t} + q\frac{\partial C}{\partial x} = \frac{\partial}{\partial x}\left(\varepsilon D\frac{\partial C}{\partial x}\right). \tag{6}$$

In this case, the macroscale dispersion is the only relevant parameter, along with the associated macroscale Péclet number.

To make a distinction between Fickian and non-Fickian transport, the analysis of concentration distribution curves is of particular interest. To analyze the step input tracer tests presented, both the time evolution of the outflow concentration [breakthrough curve (BTC)] and its time derivative (dBTC, also known as residence time distribution [48]) were considered. The dBTC corresponding to the ADE model is Gaussian, while in the case of non-Fickian transport (described for example by the DP) the dBTC presents tailing that can be described with a power-law relationship. In other words, in this latter case the slope of the dBTC curve can be described as a power-law function of time [32,49].

Pore-scale and macroscale models can be linked together by means of upscaling procedures [50,51]. In this study, pore-scale concentrations resulting from the numerical solution of Eq. (4) are upscaled as flux-averaged macroscale concentrations. In particular, when the main flow direction is aligned with the x axis of the Cartesian reference frame and the Nth sampling plane is perpendicular to this axis, the flux-average concentration at $x = x_N$ reads as

$$\bar{C}(x_N,t) = \frac{\int_A c(x_N,y,z,t)u_x(x_N,y,z)\,dy\,dz}{\int_A u_x(x_N,y,z)\,dy\,dz}, \qquad (7)$$

where A is the integration fluid area (m^2) at x_N and u_x is the longitudinal velocity component ($m\,s^{-1}$); concentrations are normalized with respect to the inlet concentration. $\bar{C}$ is comparable with the total flux F evaluated from the solutions of Eq. (5) or (6) at the same x_N (see the Appendix): thanks to a suitable fitting procedure, this comparison allows to extrapolate the parameters that characterize the system.

In order to understand the nature of the transport phenomena, a proper description of the flow field is essential: probability density functions (PDFs) of the fluid velocity (i.e., its magnitude and components) [52] are extracted from the simulation data and divided into different volume-weighted classes evaluated as volume averages. PDFs are evaluated over the whole computational volume (liquid phase volume of the porous medium).

III. NUMERICAL DETAILS

Both the numerical solution of the equations governing the pore-scale system and the preprocessing (geometry and mesh generation) were performed with OPENFOAM (version 2.3.0), an open-source computational fluid dynamics (CFD) code.

All the geometries considered were characterized by the presence of seven planes of symmetry, three perpendicular to the principal directions of the reference frame and four parallel to the main diagonals of the cube faces. Symmetries were used in this work to minimize the extent of the computational domain, as it was reduced to one fourth of the elementary cubic cell.

Figure 1 reports the original elementary cubic cells for fcc, bcc, and sic, the corresponding symmetry planes, and the reduced computational modules. The full domain was then built by repeating this fundamental module many times along the main flow direction: this much larger linear extension was necessary in order to catch the full development of the concentration plume and extract meaningful statistics, especially at larger Péclet numbers. In this study, 32 repeating modules were found to be sufficient for this purpose: a sketch of the resulting geometry is also shown in Fig. 1.

The meshing strategy was composed of two steps. First, a multiblock body-fitted approach was used so that most cells in the bulk of the domain formed a uniform Cartesian mesh, favoring convergence. The mesh near the grain surface then underwent an additional refinement, in order to fully resolve the momentum and concentration boundary layers around each grain. This strategy was found to be a good tradeoff as it resulted in acceptable computational costs, accurate numerical solutions, and code stability. More details about the meshing strategy and the grid independence of the numerical results can be found in Boccardo *et al.* [7] and Icardi *et al.* [52].

The first step in the simulation process was to solve the Navier-Stokes and continuity equations (1) and (2), using the SIMPLEFOAM solver. In order to replicate a situation where the fluid flow exhibits one predominant direction, the direction was chosen to be parallel to the x axis of the computational

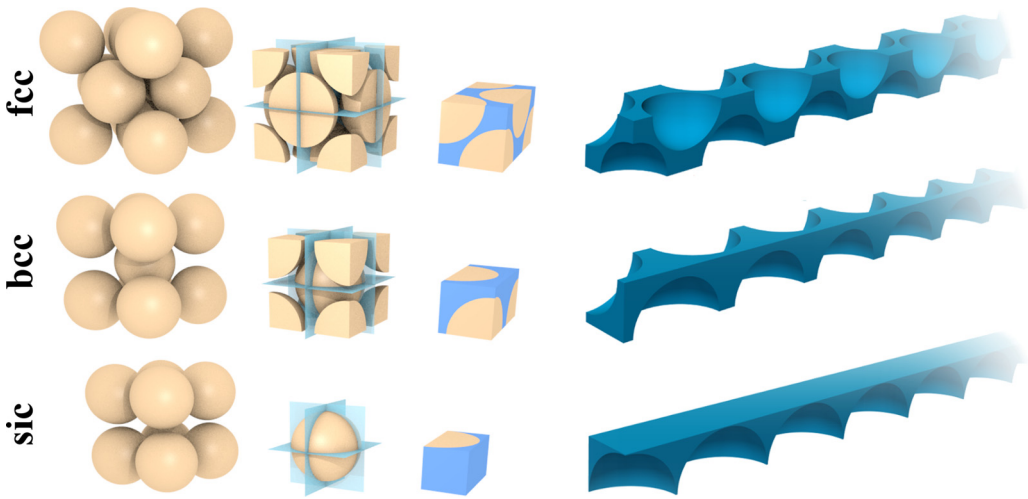

FIG. 1. Elementary cubic cells for (from top to bottom) fcc, bcc, and sic; the cells are presented with the three main planes of symmetry and the corresponding computational domain. The rightmost image in each line represents part of the structure of the whole 32-module computational domain.

TABLE I. Geometrical dimensions of the computational domains for each configuration: the periodic length ℓ, the domain length L in the x direction, and the total volume V, along with mesh cells number.

Geometry	Periodic length (m)	Length x axis (m)	Total volume (m^3)	Porosity	No. of cells
fcc	3.03×10^{-4}	9.70×10^{-3}	8.93×10^{-11}	0.4	6.91×10^{6}
bcc	2.40×10^{-4}	7.70×10^{-3}	4.46×10^{-11}	0.4	3.72×10^{6}
sic	2.03×10^{-4}	6.49×10^{-3}	3.35×10^{-11}	0.5	2.05×10^{6}

domain. Inlet and outlet zones were identified on the two opposite sides of the domain orthogonal to the x axis (see Fig. 1). A fixed pressure drop was set between these two faces, as well as the periodicity of the flow field. A symmetry condition was imposed on the remaining boundaries in order to ensure null fluid flow across them. Finally, a no-slip boundary condition $\mathbf{u} = \mathbf{0}$ was imposed on the solid grains' surface. From fluid flow simulations the velocity PDFs were extracted, together with the helicity of the fluid flow and the fluid streaklines shown in the next sections, whose visualization helps to identify the recirculation zones.

Subsequently, the advection-diffusion equation (4) was solved using the SCALARTRANSPORTFOAM solver. Since the purpose is to study the transport of a tracer, i.e., a passive (nonreactive) solute, a condition of null solute flow towards the solid was used, setting $\mathbf{n} \cdot \nabla c = \mathbf{0}$ on the grains' surface; this condition ensures that the solute does not permeate and diffuse into the solid matrix. The advective transport time τ was evaluated as $\tau = L/u$, where L is the total length of the geometry (Table I). The numerical setup then replicated a step injection of the tracer for a time equal to 5τ, followed by a flushing (i.e., injection of clear fluid carrier without solute) lasting 5τ further. To this end, at the inlet a constant concentration value was set for the first 5τ segment of the simulation, switching to a value of $c = 0$ for the flushing segment. At the outlet, a zero diffusive flux was kept for both parts of the simulation, while a symmetry boundary condition was set on the other boundaries to ensure the solute did not cross these faces.

To solve Eqs. (5) and (6), constant total fluxes were imposed at the domain boundaries: the diffusive flux was null at the outlet while it was assumed equal to the advective one at the inlet. The fitting procedure that extrapolates model parameters uses FMINCON, a constrained nonlinear solver available in the MATLAB suite: constraints were imposed in order to keep physical meaningful parameters values (e.g., porosity cannot exceed the total geometrical one).

IV. TEST CASES AND OPERATING CONDITIONS

The spherical grains composing the investigated geometries are all of equal size, with a diameter of 200 μm. Both bcc and fcc geometries were built with a porosity of 0.4, while the sic case has a porosity of 0.5 (i.e., for this last case, the minimum reasonable value to avoid copenetration between grains). The details of the investigated domain characteristics are reported in Table I. As detailed in Table II, simulations were performed under various operating conditions, always in laminar flow regime and at preasymptotic time scales. In the macroscale model β, Pe_H, and ϕ were assumed as unknown parameters: they were eventually evaluated thanks to a fitting procedure performing a least-square minimization. The residual R is given by the difference between the pore-scale simulation results $\bar{C}(x_N,t)$, obtained from Eq. (7), and the macroscale total flux $F(x_N,t)$ (details are reported in the Appendix).

Given ℓ as the length of the periodic element (see Table I), concentrations were extrapolated at a distance $x_N = N\ell$ from the inlet, where $N = \{1,2,\ldots,32\}$ is the index of the modules in each simulated geometry. The residual was then evaluated as

$$R = \sum_{N=1}^{32} \left\{ \sum_i [\bar{C}(N\ell,t_i) - F(N\ell,t_i)]^2 \right\}. \tag{8}$$

Porosities were assumed to be constant all over the domain. The geometric porosity ε was fixed and readily defined. Mobile porosity ε_m was extrapolated from the fitting and assumed constant, as was β: indeed, due to the periodicity of the flow field in each element, the size of recirculation zones is constant along the domain. Conversely, both D_H and ϕ were considered piecewise functions of the space variable: constant values were assumed over a single periodic element, but they could change from one module to the next. To describe the functional dependence of D_H and ϕ, after testing different alternatives, the following relations

$$D_H = \frac{x^c}{a + bx^c}, \tag{9}$$

$$\phi = \frac{\chi d_g}{q} = d - \frac{x^g}{e + fx^g}, \tag{10}$$

were used, where the space variable x (m) represents the distance from the injection point. The fitting parameters considered were then the seven coefficients (lowercase Latin letters from a to f) appearing in Eqs. (9) and (10). Values assumed by the piecewise functions describing the dispersion and exchange coefficients were given by $D_H(x_n)$ and $\phi(x_n)$, where $x_n = \ell(2N-1)/2$, i.e., the values of the functions in the middle of each module.

TABLE II. Operating conditions: effective velocity (u), diffusion (D_0), Reynolds (Re) and Péclet (Pe_0) numbers characterizing each operating condition.

Case	u ($\mathrm{m\,s^{-1}}$)	D_0 ($\mathrm{m^2\,s^{-1}}$)	Re	Pe_0
I	1.00×10^{-6}	4.39×10^{-12}	2.05×10^{-4}	46
II	2.50×10^{-5}	4.39×10^{-12}	5.12×10^{-3}	1142
III	1.00×10^{-4}	4.39×10^{-12}	2.05×10^{-2}	4568
IV	1.00×10^{-4}	1.10×10^{-12}	2.05×10^{-2}	18272

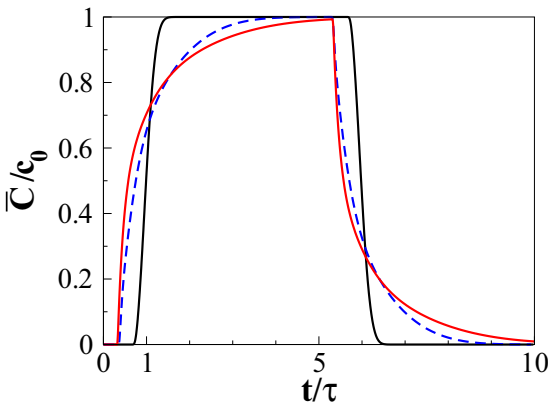

FIG. 2. Comparison among the BTCs (observed at the outlet of the domains) in the three proposed configurations (fcc, solid black curve; bcc, dashed blue curve; sic, solid red curve) for the operating condition III ($Pe_0 \simeq 4550$, $Re \simeq 2.05 \times 10^{-2}$). Time is scaled with τ.

V. RESULTS AND DISCUSSION

When considering laminar flow around spherical grains it would be expected that flow and solute transport would evolve in a similar way for different geometrical configurations (considering breakthrough times normalized for τ). This is not the case for 3D periodic porous media: a clear evidence of this is given by the comparison of the concentration displacement as presented in Figs. 2 and 3. It is apparent that significant differences emerge among BTCs and dBTCs extrapolated from both different geometrical configurations and under different operating conditions. In the fcc configuration, the BTCs are sigmoidal and the corresponding dBTCs are Gaussian, consistently with the assumption of Fickian transport; deviations from the normal distributions can be neglected since the power-law decrease is very short lived and does not significantly affect the distribution variance. Conversely, except for the operating conditions at the lowest Péclet number ($Pe_0 \simeq 45$, $Re \simeq 2.04\times10^{-4}$) where the transport can always be assumed to be Fickian, both bcc and sic geometries present an accentuated nonsigmoidal shape of the BTCs, early arrival times, and enhanced tailing. Early breakthrough times do not show dependence on the operating condition considered while tailing does since the extension and the slope of the tailing vary with the Péclet number. Figure 3 presents the dBTCs evaluated at distances of 6, 18, and 30 module lengths from the injection point, in order to observe the transition from anomalous to Fickian transport; such a transition is governed by both the geometrical configuration and the operating conditions. It is possible to notice that the bcc and the sic cases show a different behavior. The bcc at $Pe_0 \simeq 1140$ and $Re \simeq 5.10\times10^{-3}$ tends

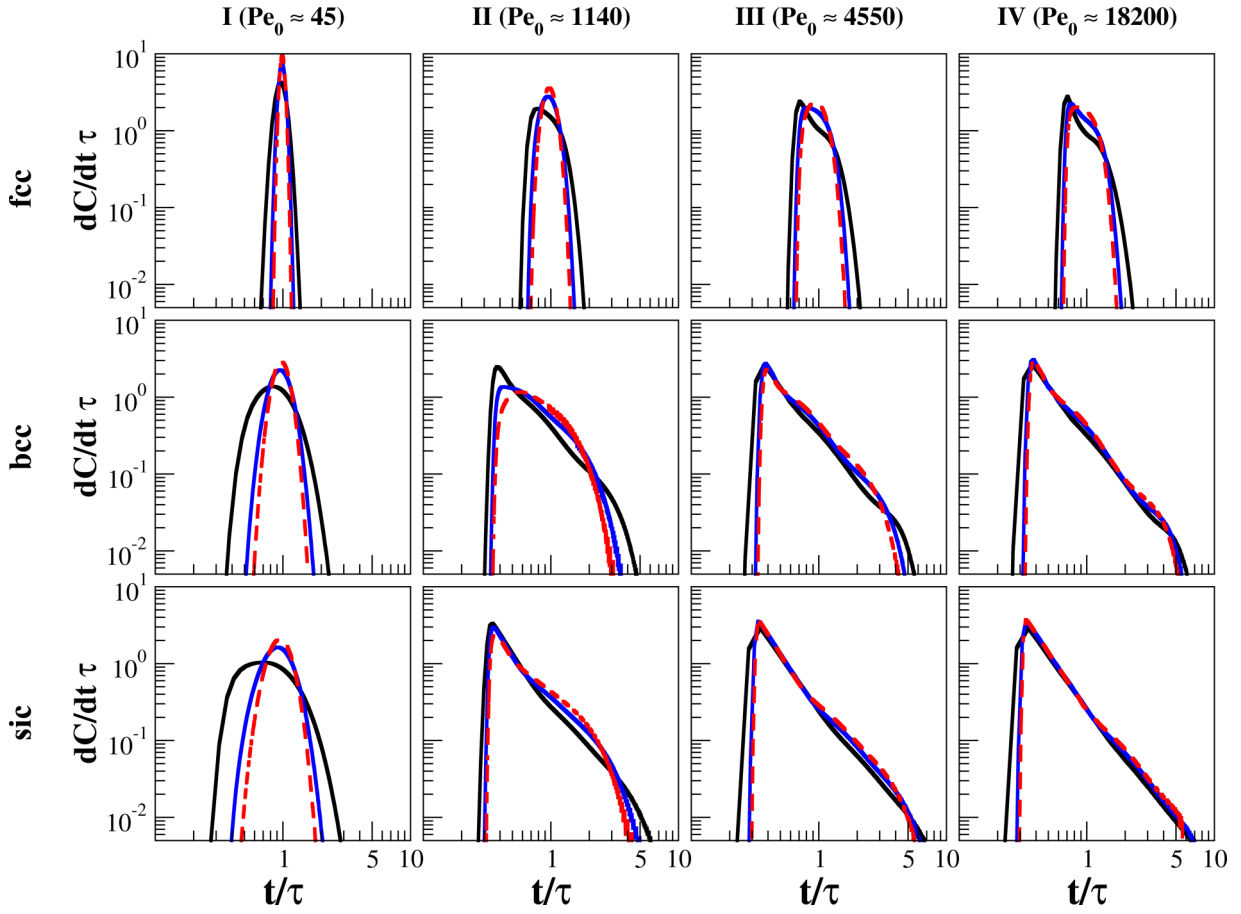

FIG. 3. dBTC curves for fcc, bcc, and sic configurations (from top to bottom) in every operating condition (I to IV from left to right); in each case, three observation points are chosen, at 6ℓ (solid black curve), 18ℓ (solid blue curve), and 30ℓ (dashed red curve), respectively, where ℓ is the length of the periodic module; times are normalized by τ relative to each curve.

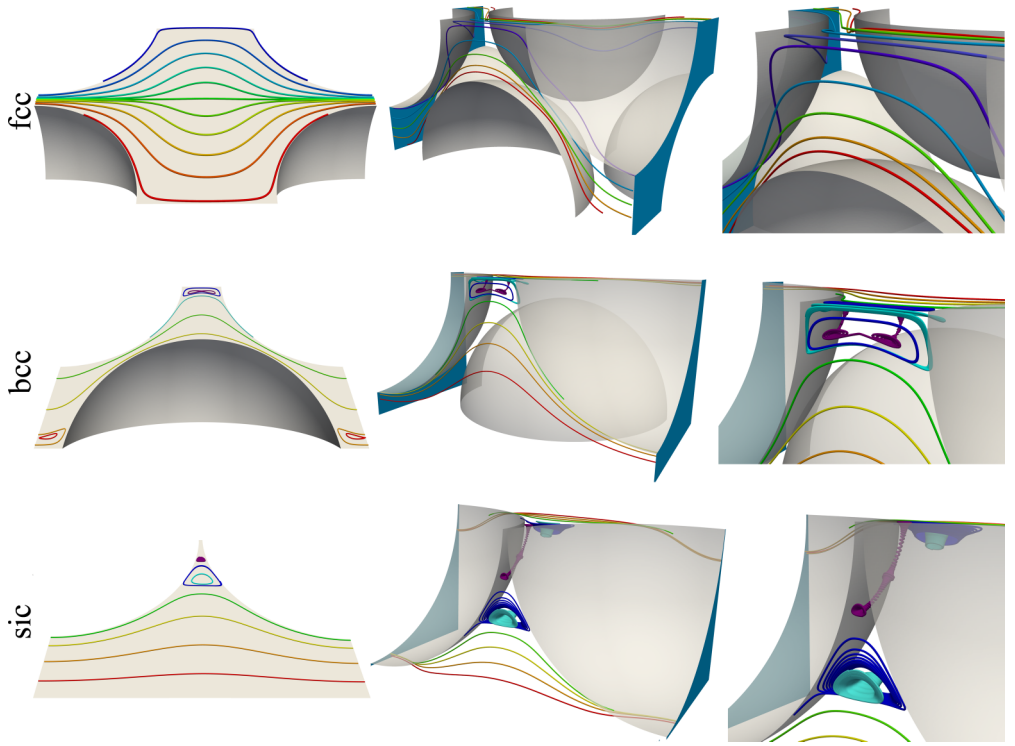

FIG. 4. Streaklines representation in fcc, bcc, and sic configurations (from top to bottom); from left to right it is possible to appreciate the behavior of streaklines in the core of the fluid domain and in-between two consecutive grains.

to a Gaussian-type shape, while this does not happen in the sic geometry. Furthermore, in the sic configuration the slope of tailing changes smoothly, while the bcc variations are greater, resulting in a series of humps, especially at high Péclet numbers.

The peculiar shape of BTCs and dBTCs (the persisting tailing in particular) can be explained by the presence of recirculation zones [37,53], that are portions of the liquid phase in which fluid elements follow annular trajectories. In the presence of recirculation, the fluid domain can be partitioned into two portions: the bulk region, characterized by high velocities usually aligned with the mean flow direction, and the recirculating region, where velocities are very low. In agreement with the observations made when analyzing concentration displacement with time, solutes in the bulk region travel down their paths quickly, appearing at the outlet earlier than the time estimated by the mean velocity, while particles entering recirculation zones are trapped there and are released only at longer times. This partition mirrors the subdivision of the domain into a mobile zone (identified by the effective porosity ε_m) and a stagnation zone, as proposed in the DP model. In order to identify the domain characteristics by its active part, it will be characterized by its effective porosity, which excludes the stagnant (i.e., recirculating) zones.

The clearest way to explain recirculation is by means of streaklines visualization. Results confirm what was suggested by the previous analysis: as depicted in Fig. 4, recirculation is evident in the bcc and the sic cases, while it does not appear in the fcc configuration. Figure 4 offers different perspectives of the streaklines: it shows both the presence of a series of nested recirculating streaklines and the differences in flow structures between bcc and sic cases. The bcc configuration presents a series of twin spirals at the core of the recirculation zone spinning in opposite directions, whereas in the sic geometry only singular annular recirculating paths are present. Moreover, in the bcc configuration there is only one set of nested recirculating streaklines, while in the sic geometry there are three distinct recirculation zones, one surrounding the other: at the core of recirculation the streams are stretched, while in the intermediate and external recirculation zones streaklines have a well defined shape. Differences in flow topology are due to the different spatial distribution of the grains, and in particular to the different distance between two consecutive grains. Other interesting features can be appreciated from the lateral view: streaklines follow elongated helical trajectories, assume a full 3D structure, and are symmetrical with respect to the symmetry planes of the geometry. A point worth making is that, intuitively, flow structure would also be directly influenced by the medium porosity, with lower porosities and narrower channels being linked to higher probability of stagnant or recirculation zones arising. In order to confirm our assumption regarding the fundamental difference between fcc and bcc and sic models, we performed a fluid flow simulation on a fcc model with a porosity $\varepsilon = 0.29$. This is the lowest possible value obtainable while still avoiding solid grain interpenetration: the difference between this value and Kepler's conjecture theoretical close-packing porosity of $\varepsilon = (1 - \frac{\pi}{3\sqrt{2}}) \approx 0.26$ is due to the limits of the mesh spatial discretization. We then analyzed the resulting flow field with both the quantitative and qualitative methods presented thus far, confirming that even in this limit case, the particular geometry of the fcc model inhibits the formation of recirculation fluid zones, ultimately responsible for the anomalous transport behavior in the bcc and sic cases.

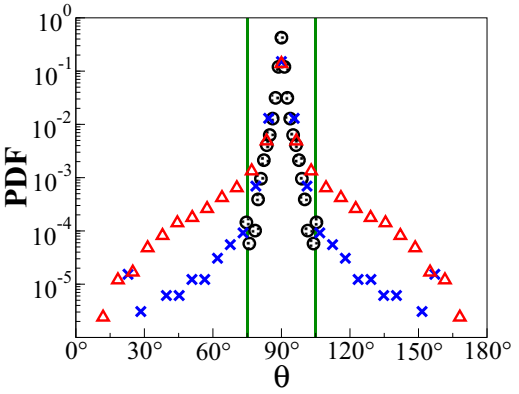

FIG. 5. Distribution of the angle θ, defined in Eq. (3), between velocity **u** and vorticity $\boldsymbol{\omega}$ vectors in the three proposed configurations (fcc, black circles; bcc, blue crosses; sic, red triangles), for the operating conditions III–IV($\mathrm{Re} \simeq 2.05 \times 10^{-2}$).

For example, the streaklines visualization for this limit case resulted in a flow structure which is in every way similar to the one presented in Fig. 4, relative to a higher porosity $\varepsilon = 0.4$.

Other than defining the shape of the recirculation zones, the quantification of their extension helps to evaluate the effective porosity of the medium. It is straightforward to identify the portion of volume occupied by recirculation: for example, this can be done evaluating the velocity magnitude and tracing different isosurfaces. Recirculation seems to be well confined by the isosurface that corresponds to the 1% of the mean velocity magnitude. This result holds true for both bcc and sic geometries under all the operating conditions. Then, given the volume occupied by the grains, the evaluation of the volume included between the boundaries and the isosurface leads to the calculation of the effective porosity. This procedure implicitly takes into account also a thin layer of fluid attached to the grains, influenced by the no-slip boundary condition. The same analysis applied to the fcc cases confirms once more that the presence of recirculation and stagnant zones can be practically ignored. The values of ε_m obtained are 0.3999, 0.3975, and 0.4710 for fcc, bcc, and sic, respectively, and since they do not change varying the operating conditions, this analysis confirms the fluid dynamic similarity between different Reynolds numbers in laminar regime [recall that the geometrical porosity is equal to 0.4 for both fcc and bcc, while it is 0.5 in the SIC configuration (see Table I)].

So far, this section has focused on a qualitative perspective. However, when the knowledge of the flow field is obtainable, but streaklines visualization is not a viable tool, it is fundamental to quantitatively detect the presence of recirculation zones. In this light, useful insights can be gained by the analysis of velocity PDFs. Considering the angle θ formed by velocity and vorticity, Fig. 5 shows the clear distinction between the fcc geometry and the cases in which recirculation

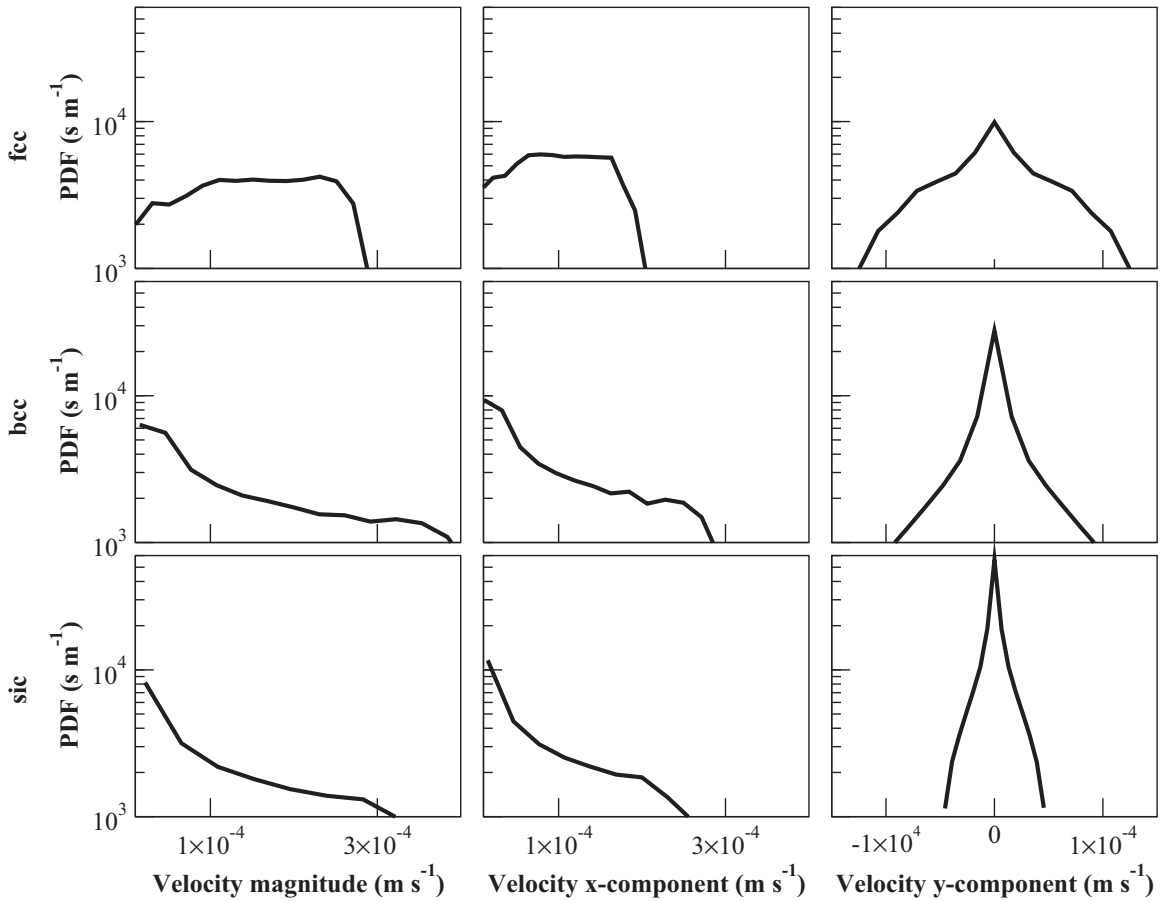

FIG. 6. PDFs of velocity magnitude, velocity x and y components (from left to right) for the fcc, bcc, and sic configurations (from top to bottom), operating conditions III–IV($\mathrm{Re} \simeq 2.05 \times 10^{-2}$).

is present: in the former configuration, θ ranges from 75° to 105°, while the values obtained for bcc and sic span a much broader range. Returning to a qualitative analysis, the correlation between θ and recirculation is confirmed since cells in which $\theta \in [0°,75°]$ or $\theta \in [105°,180°]$ correspond to the portion of the domain where streaklines bend to follow their helical trajectories. Regarding the velocity distribution, in each case the PDFs of velocity transversal components (i.e., along y and z directions) are qualitatively equal since simulations were carried out under steady-state conditions in isotropic media. Furthermore, the distributions of velocity's transversal components are symmetrically distributed around the mean that, given the symmetry boundary conditions adopted, is equal to zero [52]. More striking results emerge from the analysis of both the velocity magnitude and the velocity longitudinal component. Figure 6 provides the comparison among the investigated geometries. The distributions obtained for each geometry are quite different from the case of a cylindrical tube, which is a useful reference case as it represents the geometrically homogeneous limit [36]. The fcc cases have almost uniform distributions for velocity magnitude and x component, centered on the mean values, whereas in both the bcc and sic cases the distributions are skewed towards low velocities. Regarding the magnitude and x component of velocity, both bcc and sic cases show variances greater than those of the fcc case. This, together with the prominence of low velocity and negative x-velocity values, is consistent with the presence of recirculation: fluid particles have to travel along tortuous trajectories with low velocities and this causes the spreading of the PDF values around the mean [41].

Further analysis shows that in the fcc geometry the volumes of fluid engaged in low velocities are small and are located around the grains' surface. This evidence is consistent with the no-slip boundary condition imposed, but it does not hold true in both bcc and sic geometries, where regions of fluid characterized by low velocities were also detected in the bulk of the domain. These results confirm once more that the arrangement of the spherical collectors may cause particular fluid structures to develop, extending the "stagnant" zone far beyond the grains' surface.

The next step would be to find a connection between one particular arrangement and the resulting fluid structure, ultimately with the purpose of predicting the possible onset of recirculating zones and possibly their magnitude. At first, a possible way to describe the geometrical structure, and specifically how it evolves along the direction of the fluid flow, is the analysis of the cross-section area. Area values are shown in Fig. 7, along with graphical representations making the analysis and the features of each model more clear.

However, from this characterization it is not straightforward to identify a general criterion (i.e., a rule that can be applied to each and every structure) by which to predict the presence of stagnant zones. In this perspective, it appears necessary to perform a complete simulation campaign to further investigate the flow field.

Having discussed how to detect the presence of recirculation zones, we also addressed how to account for their influence in the construction of a macroscale model that describes the observed anomalous transport. A common methodology for the analysis of anomalous transport is that based on the CTRW

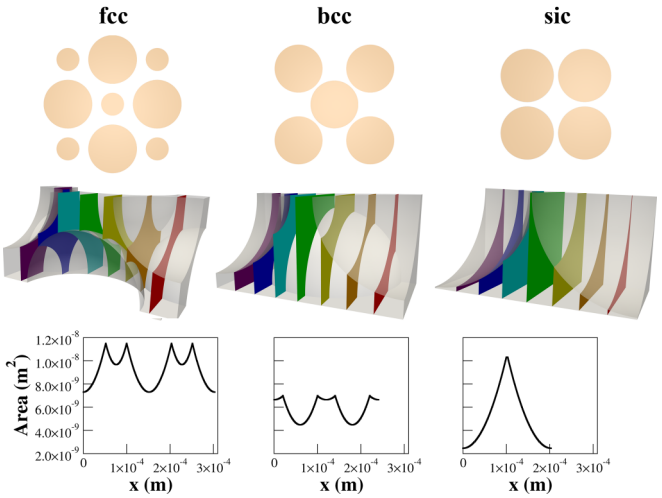

FIG. 7. Spatial evolution of the cross-section area in fcc, bcc, and sic geometries (from left to right). Top: frontal view of the solid grains within the cubic cell. Middle: slices exemplifying the averaging process along the x axis for the calculation of the cross-section area. Bottom: evolution of the cross-section area along the main flow direction (the x axis). Porosity is that used in the simulation campaign.

theory. Nevertheless, we present a different approach based on the DP model, as it can be readily implemented in our in-house developed software.[1]

From the results presented in the previous sections, it is clear that the classical ADE cannot be employed in the bcc and the sic cases, whereas it is a reliable model for the fcc cases. Thus, the DP model is adopted to describe the bcc and the sic cases, identifying the immobile and stagnant zones in the model with the recirculation zones present in the two configurations. Dispersion and porosity were set as model parameters for the ADE, while dispersion, mobile porosity, and exchange coefficient were chosen for the DP. Both the D_H and ϕ are known to be dependent not only on the geometrical properties of the medium, but also on the operating conditions considered, since they are linked to the velocity field and to the diffusion coefficient. To make a reliable comparison between different cases, the dimensionless form of each parameter was considered: $\beta = \varepsilon_m/\varepsilon$, $\phi = \chi d_g/q$, and $\mathrm{Pe}_H = q d_g/(\varepsilon_m D_H)$. Even so, results are presented for D_H, as it is by itself a relevant parameter in practical applications.

Given the very long transition time to reach the asymptotic regime in the case of bcc and sic geometries, it makes sense to describe D_H and ϕ with a functional form that varies in space, as detailed in Eq. (9). The functional form proposed is able to reproduce a linear dependence on the space variable while also satisfying $D_H(x \to \infty) = 1/b, \phi(x \to \infty) = d - 1/g \; \forall \; d,g$. This last feature implies that far from the injection point, the parameters can assume constant values predicting the eventual reaching of the asymptotic regime.

From the data, it is apparent that D_H, ϕ, and β strongly depend on the pore-scale Péclet number Pe_0. Regarding D_H, in each geometrical configuration the lower is Pe_0, the lower

[1] http://areeweb.polito.it/ricerca/groundwater/software/MNMs.php

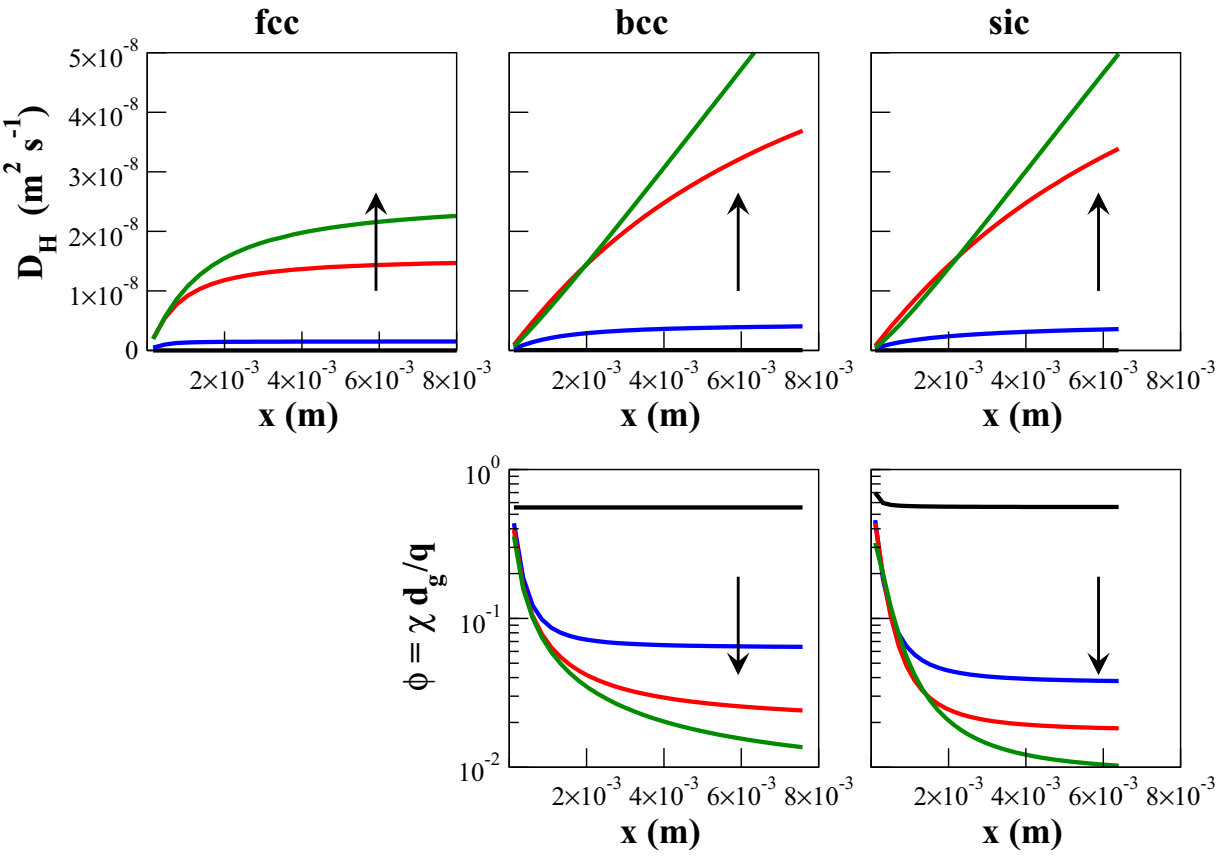

FIG. 8. Dispersion and exchange coefficient values obtained from the multiple curve fitting. Arrows indicate increasing Pe_0, from operating condition I (black, $Pe_0 \simeq 46$, $Re \simeq 2.04 \times 10^{-4}$) to IV (green, $Pe_0 \simeq 18\,200$, $Re \simeq 2.04 \times 10^{-2}$). The exchange coefficient for fcc cases is not presented since this geometry's data are fitted against the ADE model, where no exchange coefficient is needed.

is the dispersion, as shown in Fig. 8. In particular, under the operating condition I ($Pe_0 \simeq 45$, $Re \simeq 2.04 \times 10^{-4}$), D_H can be considered as constant since after about two modules it reaches an asymptotic value, equal to 7.77×10^{-12}, 4.96×10^{-11}, and 2.78×10^{-11} $m^2\,s^{-1}$ in fcc, bcc, and sic cases, respectively. At higher Pe_0 it is possible to highlight a different behavior depending on the geometrical configuration and the presence of recirculation. Indeed, under all the explored operating conditions, fcc cases see dispersion quickly reaching a well defined asymptotic value, whereas in both bcc and sic geometries the higher is the Pe_0, the more the dispersion trend can be accurately described by a linear function of space. Overall, the transition to the linear dependence is in agreement with the analysis of the dBTCs and the nature of transport: it can be observed that an asymptote is reached in those cases presenting a Gaussian-type dBTC. Regarding the evaluation of Pe_H at the domain outlet, the higher is the pore-scale Péclet, the lower is the macroscale one.

For completeness, this type of analysis is absolutely equivalent to the possibly more common evaluation of the evolution in time of the solute particles mean-square displacement $\langle(\Delta x)^2\rangle \sim t^\eta$, that results in a nonlinear relationship in the case of anomalous transport (i.e., $\eta \neq 1$). The evolution of $\langle(\Delta x)^2\rangle$ as a function of time requires an integration over very long spatial scales of the solute concentration (by means of calculating the second moment of the solute concentration distribution); for the presented simulations this would be quite an impractical choice. Nonetheless, taking into account the numerical issues and thus considering only a limited time scale in our results, the outcome of such an analysis is coherent with the ones just presented for the full spatial scale, as reported in Fig. 8, correctly identifying the transition between preasymptotic and asymptotic regimes for all the investigated cases.

With respect to the dimensionless exchange coefficient ϕ, it also shows a direct correlation with Pe_0: ϕ decreases increasing Pe_0, as depicted in Fig. 8. Under all the operating conditions proposed, ϕ reaches a well defined asymptotic value; as in the case of dispersion, the convergence to the asymptote depends on Pe_0, and the lower is Pe_0 the faster is the convergence. When ϕ can be assumed as constant over an extended portion of the domain, especially at low Pe_0, it means that diffusion has sufficient time to smooth out the gradient due to advection, and the difference of concentration between mobile and immobile regions is attenuated.

Special attention must be paid to the fitted values of mobile and immobile porosity. In the fcc configuration, the fitted value of ε is equal to the geometrical one, leading to $\beta = 1$ under each operating condition. On the other hand, in both bcc and sic cases the resulting values of β are lower than 0.5, with the only exception of operating condition I. This indicates that immobile regions extend to more than half of the liquid region, and the fitted values of ε_m are substantially lower than

those evaluated on the basis of the flow field analysis. The predominance of the immobile region is ascribable to the fact that the dimensionality reduction (suffered when upscaling to a one-dimensional system) implicitly conceals vertical gradients of concentration appearing in 3D pore-scale simulations, in particular at high Pe_0, causing a numerical amplification of the dimension of the immobile region to take into account all the concealed concentration gradients. This hypothesis is confirmed by the finding that higher values of mobile porosity are observed under the operating condition I, where the vertical gradients are already attenuated due to the balance between diffusion and advection.

VI. CONCLUSIONS

In this work, solute transport in periodic porous media was investigated, paying specific attention to the role of the spatial distribution of the grains: the comparison among three geometries with equal grain size but different grain spatial disposition allows to appreciate significant differences in both the flow field and in the solute transport.

This study provides the correlation between the geometrical configuration and the onset of recirculation zones in laminar flow conditions. Furthermore, the analysis of the outflow concentration curves supports the idea of the correlation between recirculation zones and anomalous transport. In particular, it is shown that the presence of recirculation correlates to the enhanced power-law tailing effect. To characterize recirculation, 3D visualization of the flow field allowed to qualitatively measure the extension of recirculation zones and to highlight how the different configurations result in different streakline paths, even at equal Reynolds numbers and grain size. This post-processing analysis was performed along with a probability density function analysis of the flow field, in order to provide a quantitative tool to detect the presence of recirculation zones. The combined analysis of the angle θ (between vorticity and velocity vectors) and the PDFs of velocity (mainly magnitude and its x component) was then proposed: the differences among the three geometries were used to set apart cases with or without recirculation. The predominance of $\theta \simeq 0^\circ$ and $\theta \simeq 180^\circ$ and a velocity PDF skewed toward very low velocities were identified as the main features indicating the onset of recirculation. An initial attempt was made to characterize the differences among different packing configurations, pertaining to the individuation of the structural features causing the onset of recirculation. A more complete characterization based on a thorough numerical campaign will be addressed in future works.

Furthermore, since the ultimate purpose of pore-scale simulations is to provide the characterization of macroscale parameters of interest, the insight gained by the study of recirculation zones was used to fit numerical data with a proper macroscale model. In particular, two different macroscale models were considered: the classical advection-dispersion model, adopted for the fcc geometry, and the dual-porosity model for bcc and sic. This latter choice has been made assuming that recirculation zones can be described as stagnation zones. The effectiveness of this choice was confirmed by the results of this study, as in absence of recirculation they are in good agreement with the theoretical results expected for an ADE model; in particular, the porosity value equals the geometrical one. The spatial variation of D_H can be explained analyzing the spatial evolution of the dBTC curves, presenting deviations from the Gaussian shape that are gradually smoothed along the domain.

Concerning the dual-porosity model, the results show a clear dependence on the pore-scale Péclet number, showing a linear growth of D_H with respect to the space variable. On the other hand, the exchange coefficient can be assumed as constant, given a sufficiently extended domain.

To conclude, recirculation zones in porous media are clearly linked to non-Fickian transport behavior and may (nonintuitively) arise even in laminar flow conditions: pore-scale simulations are a valuable tool for their identification and for the subsequent determination of effective macroscale transport parameters.

ACKNOWLEDGMENTS

We acknowledge the CINECA award under the ISCRA initiative and HPC@POLITO (http://www.hpc.polito.it) for the availability of high performance computing resources and support.

APPENDIX

This Appendix provides details concerning the calculation of relevant quantities and details of the implemented macroscale equations. Providing that the main flow direction is parallel to the x axis and given the boundary conditions imposed (as detailed in Sec. III), the effective velocity u ($\mathrm{m\,s^{-1}}$) is computed as

$$u = \frac{\int_V u_x \, dv}{V}, \tag{A1}$$

in which u_x is the velocity component ($\mathrm{m\,s^{-1}}$) in the main flow direction and V is the total liquid volume ($\mathrm{m^3}$). On the other hand, the Darcyan velocity q ($\mathrm{m\,s^{-1}}$), also known as superficial velocity, is evaluated as

$$q = \frac{\int_A u_x dy \, dz}{A_{\mathrm{tot}}}, \tag{A2}$$

where the areas A and A_{tot} are orthogonal to the main flow direction ($\mathrm{m^2}$); in particular, A is the integration area pertaining liquid phase and A_{tot} is the total area (liquid and solid).

The dimensionless form of Eqs. (5) and (6) has been obtained following the work of Nkedi-Kizza *et al.* [54], with the following assumptions:

$$\begin{aligned} c_m &= \mathsf{C}_m \, c_0, \quad c_{im} = \mathsf{C}_{im} \, c_0, \\ x &= \mathsf{X} \, d_g, \quad t = \mathsf{T} \, \frac{d_g \, \varepsilon}{q}, \end{aligned} \tag{A3}$$

where c_0 is the reference concentration and the characteristic length is equal to the grains' diameter d_g. To obtain a dimensionless time, the geometrical porosity is used in both the DP

and the ADE models. Adopting Eq. (A3), the dimensionless form of Eq. (5) reads as

$$\beta\frac{\partial \mathsf{C}_m}{\partial \mathsf{T}}+\frac{\partial \mathsf{C}_m}{\partial \mathsf{X}}=\frac{\partial}{\partial \mathsf{X}}\left(\frac{1}{\mathrm{Pe}_H}\frac{\partial \mathsf{C}_m}{\partial \mathsf{X}}\right)-\phi(\mathsf{C}_m-\mathsf{C}_{im}),$$

$$(1-\beta)\frac{\partial \mathsf{C}_{im}}{\partial \mathsf{T}}=\phi(\mathsf{C}_m-\mathsf{C}_{im}), \tag{A4}$$

where $\beta=\varepsilon_m/\varepsilon$, $\mathrm{Pe}_H=qd_g/(\varepsilon_m D_H)$, and $\phi=\chi d_g/q$. Similarly, the dimensionless form of Eq. (6) is

$$\frac{\partial \mathsf{C}}{\partial \mathsf{T}}+\frac{\partial \mathsf{C}}{\partial \mathsf{X}}=\frac{\partial}{\partial \mathsf{X}}\left(\frac{1}{\mathrm{Pe}_H}\frac{\partial \mathsf{C}}{\partial \mathsf{X}}\right). \tag{A5}$$

In the evaluation of the residual for the fitting algorithm, the macroscale flux is needed. The total flux reads as

$$F(x_N,t)=\frac{q\,C_m(x_N,t)-\varepsilon_m\,D\nabla C_m(x_N,t)}{q} \tag{A6}$$

for the dual-porosity model (5). It is instead defined as

$$F(x_N,t)=\frac{q\,C(x_N,t)-\varepsilon\,D\nabla C(x_N,t)}{q} \tag{A7}$$

for the classical advection-dispersion model (6).

[1] M. M. Krol, A. J. Oleniuk, C. M. Kocur, B. E. Sleep, P. Bennett, Z. Xiong, and D. M. O'Carroll, Environ. Sci. Technol. **47**, 7332 (2013).
[2] E. D. Vecchia, M. Luna, and R. Sethi, Environ. Sci. Technol. **43**, 8942 (2009).
[3] I. Gunn and A. W. Woods, J. Fluid Mech. **672**, 109 (2011).
[4] T. Tosco, D. Marchisio, F. Lince, and R. Sethi, Transp. Porous Media **96**, 1 (2013).
[5] R. C. Holleman and M. T. Stacey, J. Fluid Mech. **736**, 130 (2013).
[6] M. Rolle, G. Chiogna, D. L. Hochstetler, and P. K. Kitanidis, J. Contam. Hydrol. **153**, 51 (2013).
[7] G. Boccardo, F. Augier, Y. Haroun, D. Ferré, and D. L. Marchisio, Chem. Eng. J. **279**, 809 (2015).
[8] F. Augier, F. Idoux, and J. Delenne, Chem. Eng. Sci. **65**, 1055 (2010).
[9] S. Bensaid, D. Marchisio, D. Fino, G. Saracco, and V. Specchia, Chem. Eng. Sci. **154**, 211 (2009).
[10] M. Prodanović, W. B. Lindquist, and R. S. Seright, J. Colloid Interface Sci. **298**, 282 (2006).
[11] R. Kolakaluri, E. Murphy, S. Subramaniam, R. Brown, and R. Fox, AIChE J. **61**, 3594 (2015).
[12] S. Tenneti, R. Garg, and S. Subramaniam, Int. J. Multiphase Flow **37**, 1072 (2011).
[13] X. Shi, M. Prodanović, J. Holder, K. Gray, and D. DiCarlo, J. Pet. Sci. Eng. **112**, 88 (2013).
[14] Q. A. Pankhurst, J. Connolly, S. Jones, and J. Dobson, J. Phys. D: Appl. Phys. **36**, R167 (2003).
[15] A. C. Gordon, R. J. Lewandowski, R. Salem, D. E. Day, R. A. Omary, and A. C. Larson, J. Vasc. Intervent. Radiol. **25**, 397 (2014).
[16] M. Prodanović, W. Lindquist, and R. Seright, Adv. Water Resour. **30**, 214 (2007).
[17] F. Messina, T. Tosco, and R. Sethi, Water Resour. Res. **52**, 5492 (2016).
[18] F. Messina, D. L. Marchisio, and R. Sethi, J. Colloid Interface Sci. **446**, 185 (2015).
[19] A. Grillo, M. Lampe, and G. Wittum, Computing and Visualization in Science **13**, 287 (2010).
[20] J. Bear, *Dynamics of Fluids in Porous Media* (Dover, New York, 1988).
[21] T. R. Brosten, J. Fluid Mech. **732**, 687 (2013).
[22] G. Taylor, Proc. R. Soc. London, Ser. A **219**, 186 (1953).
[23] R. Aris, Proc. R. Soc. London, Ser. A **235**, 67 (1956).
[24] T. Perkins and O. Johnston, Soc. Pet. Eng. J. **3**, 70 (1963).
[25] J. Carrera, X. Sánchez-Vila, I. Benet, A. Medina, G. Galarza, and J. Guimerà, Hydrogeol. J. **6**, 178 (1998).
[26] J. Delgado, Heat Mass Transfer **42**, 279 (2006).
[27] R. Haggerty and S. M. Gorelick, Water Resour. Res. **31**, 2383 (1995).
[28] K. Coats, B. Smith *et al.*, Soc. Pet. Eng. J. **4**, 73 (1964).
[29] M. T. Van Genuchten and P. Wierenga, Soil Sci. Soc. Am. J. **40**, 473 (1976).
[30] D. R. Lester, G. Metcalfe, and M. G. Trefry, Phys. Rev. E **90**, 063012 (2014).
[31] M. Sahimi, Phys. Rev. E **85**, 016316 (2012).
[32] S. P. Neuman and D. M. Tartakovsky, Adv. Water Resour. **32**, 670 (2009).
[33] B. Berkowitz and H. Scher, Phys. Rev. E **57**, 5858 (1998).
[34] O. Silva, J. Carrera, M. Dentz, S. Kumar, A. Alcolea, and M. Willmann, Hydrol. Earth Syst. Sci. **13**, 1399 (2009).
[35] G. M. Porta, B. Bijeljic, M. J. Blunt, and A. Guadagnini, Geophys. Res. Lett. **42**, 7537 (2015).
[36] B. Bijeljic, A. Raeini, P. Mostaghimi, and M. J. Blunt, Phys. Rev. E **87**, 013011 (2013).
[37] D. Bolster, Y. Méheust, T. Le Borgne, J. Bouquain, and P. Davy, Adv. Water Resour. **70**, 89 (2014).
[38] T. Le Borgne, D. Bolster, M. Dentz, P. Anna, and A. Tartakovsky, Water Resour. Res. **47** (2011).
[39] A. Davis, M. O'Neill, J. Dorrepaal, and K. Ranger, J. Fluid Mech. **77**, 625 (1976).
[40] S. Taneda, J. Phys. Soc. Jpn. **46**, 1935 (1979).
[41] R. Hill and D. Koch, J. Fluid Mech. **465**, 59 (2002).
[42] T. H. Wegner, A. J. Karabelas, and T. J. Hanratty, Chem. Eng. Sci. **26**, 59 (1971).
[43] A. Zick and G. Homsy, J. Fluid Mech. **115**, 13 (1982).
[44] L. Snyder and W. Stewart, AIChE J. **12**, 167 (1966).
[45] M. Rolle, D. Hochstetler, G. Chiogna, P. K. Kitanidis, and P. Grathwohl, Transp. Porous Media **93**, 347 (2012).
[46] H. K. Moffatt, J. Fluid Mech. **35**, 117 (1969).
[47] A. Einstein, Ann. Phys. (Berlin) **322**, 549 (1905).
[48] H. S. Fogler, *Essentials of Chemical Reaction Engineering* (Pearson Education, Saddle River, NJ, 2010).

[49] B. Berkowitz, A. Cortis, M. Dentz, and H. Scher, Rev. Geophys. **44**, RG2003 (2006).
[50] D. L. Hochstetler, M. Rolle, G. Chiogna, C. M. Haberer, P. Grathwohl, and P. K. Kitanidis, Adv. Water Resour. **54**, 1 (2013).
[51] I. Battiato and D. Tartakovsky, J. Contam. Hydrol. **120**, 18 (2011).
[52] M. Icardi, G. Boccardo, D. L. Marchisio, T. Tosco, and R. Sethi, Phys. Rev. E **90**, 013032 (2014).
[53] M. B. Cardenas, Geophys. Res. Lett. **35**, L18402 (2008).
[54] P. Nkedi-Kizza, J. Biggar, H. Selim, M. T. Van Genuchten, P. Wierenga, J. Davidson, and D. Nielsen, Water Resour. Res. **20**, 1123 (1984).